

Two-magnon excitations in resonant inelastic x-ray scattering studied by spin-density-wave formalism

Takuji Nomura^{1,*}

¹*Synchrotron Radiation Research Center, National Institutes for Quantum and Radiological Science and Technology, SPring-8, 1-1-1 Kouto, Sayo, Hyogo 679-5148, Japan*

(Dated: January 23, 2017)

We study two-magnon excitations in resonant inelastic x-ray scattering (RIXS) at the transition-metal K -edge. Instead of working with effective Heisenberg spin models, we work with a Hubbard-type model (d - p model) for a typical insulating cuprate La_2CuO_4 . For the antiferromagnetic ground state within the spin-density-wave (SDW) mean-field formalism, we calculate the dynamical correlation function within the random-phase approximation (RPA), and then obtain two-magnon excitation spectra by calculating the convolution of it. We propose a new microscopic mechanism of two-magnon RIXS, based on the Hund's rule coupling J_{sd} between the $1s$ and $3d$ electrons at Cu sites. A pair of magnons is excited through second-order processes in J_{sd} . Calculated momentum dependence of RIXS spectra agrees well with experimental one. A notable difference from previous calculations based on the Heisenberg spin models is that RIXS spectra have a sizable two-magnon weight at the zone center, which may be hidden by or subtracted with the elastic line in experiments.

PACS numbers: 74.72.-h, 74.72.Cj, 75.10.Lp, 78.70.Ck

I. INTRODUCTION

Resonant inelastic x-ray scattering (RIXS) at the transition-metal absorption edges is a promising powerful tool to detect various elementary excitations in strongly correlated electron systems^{1,2}. Particularly, the RIXS technique utilizing the transition-metal K - or L -edge x-rays can probe momentum dependence of elementary excitations such as charge³⁻⁵, orbital^{6,7}, and magnon excitations^{8,9}. To analyze theoretically such momentum-dependent excitations in RIXS, various effective theoretical methods have been adopted, e.g., exact diagonalization^{10,11}, perturbation expansion¹²⁻¹⁴, ultra-short life-time expansion^{15,16}, dynamical mean-field theory (DMFT)¹⁷.

In x-ray scattering with linearly polarized x-rays, the total spin moment is conserved, if effects of the spin-orbit coupling are negligible. Therefore, in contrast to neutron scattering, only an even number of magnons can be excited, whereas an odd number of magnons are prohibited to be excited. In fact, excitations with 500 meV energy and characteristic momentum dependence were observed in the Cu K -edge RIXS for La_2CuO_4 ^{18,19}, and have been identified as two-magnon excitations, based on the agreement with theoretical calculations²⁰⁻²⁴. In those previous theoretical works they adopted Heisenberg spin Hamiltonians and the spin-wave (SW) approximation.

A large number of theoretical studies on two-magnon excitations have been done in the context of Raman light scattering over several decades²⁵⁻³⁵. The essential microscopic process in those studies is the inter-site spin exchange induced by the inter-site Coulomb interaction, and can be described effectively by the so-called Fleury-Loudon (FL) Hamiltonian²⁵:

$$H_{FL} = \alpha \sum_{\langle i,j \rangle} [\mathbf{e} \cdot \mathbf{r}_{ij}] [\mathbf{e}' \cdot \mathbf{r}_{ij}] \mathbf{s}_i \cdot \mathbf{s}_j, \quad (1)$$

where α is a constant, \mathbf{s}_i is the spin operator at site i , \mathbf{e} and \mathbf{e}' are the electric-field vectors of emitted and absorbed rays, and \mathbf{r}_{ij} is a coordinate vector connecting magnetic ion sites i and j . The FL Hamiltonian can be incorporated into Heisenberg spin Hamiltonians as perturbation with ease. In calculations with the FL Hamiltonian, one can reproduce the observed characteristic lineshapes of two-magnon Raman spectra by taking account of magnon-magnon interactions, which crucially evidenced the importance of magnon-magnon interactions²⁶⁻³⁰. The FL Hamiltonian has been derived microscopically also from a Hubbard Hamiltonian in the large- U limit, being intended for the high- T_c cuprates^{32,34}.

Two-magnon excitations in RIXS should be distinguished from those in Raman light scattering, since the core hole can play an essential role in the intermediate state. We need to consider excitation processes in the presence of a $1s$ core hole at a transition-metal site in the intermediate state, which are not involved in Raman light scattering. A microscopic mechanism of two-magnon excitations in K -edge RIXS was before proposed by van den Brink²¹. He took account of virtual inter-site hopping processes to screen the $1s$ hole created in the intermediate state of RIXS, and thereby calculated the modification to the antiferromagnetic Heisenberg spin exchange J around the $1s$ core hole. The modified exchange integral between the excited site and neighboring sites induces inter-site spin exchange excitations between those sites, and consequently two magnons are generated before the $1s$ hole is finally annihilated. Hereafter, we refer to this mechanism as the inter-site exchange mechanism in two-magnon RIXS. In Ref. 20, Nagao and Igarashi incorporated this mechanism into the previous perturbative framework developed by the author and Igarashi. They replaced a ladder of electron and hole propagators in Ref. 13 with a ladder of magnon propagators, and calculated the dynamical correlation function by us-

ing the SW approximation and including the magnon-magnon interaction within $1/S$ expansion. The inter-site exchange mechanism seems to explain well the experimental observations so far in La_2CuO_4 ^{20,21,24}.

A central aim of the present work is to describe two-magnon excitations in K -edge RIXS using an itinerant Hubbard-type model (d - p model) and the spin-density-wave (SDW) formalism, instead of using a Heisenberg spin model and the SW approximation. It is less clear how we can adapt the above mentioned inter-site exchange mechanism to our itinerant-model calculation. Alternatively, we propose a new microscopic mechanism of two-magnon excitations based on the Hund's coupling between the $1s$ and d orbitals at transition-metal sites as explained in detail in the next section. This new mechanism is another natural way of extending our previous perturbative formulation to explain the two-magnon RIXS spectra, and can lead to the same or even larger magnitude of two-magnon RIXS spectra than the inter-site exchange mechanism, as we shall argue.

II. THEORETICAL FRAMEWORK

A. Hamiltonian for K -edge RIXS and s - d Hund's coupling mechanism

To be specific, hereafter we restrict our discussion to a typical copper oxide La_2CuO_4 , although our discussion below is applicable also to other transition-metal compounds. To describe the electron dynamics in RIXS, we use the following Hamiltonian:

$$H = H_d + H_s + H_{sd} + H_p + H_x. \quad (2)$$

We present each term explicitly in the following. H_d describes the electronic states near the Fermi energy (E_F). We take a Hubbard-type Hamiltonian (d - p model) for the $\text{Cu}3d_{x^2-y^2}$ and $\text{O}2p_{x,y}$ orbitals in a single CuO_2 layer:

$$H_d = H_0 + H', \quad (3)$$

$$\begin{aligned} H_0 = & \sum_i \sum_\sigma \varepsilon_d d_{i\sigma}^\dagger d_{i\sigma} + \sum_a \sum_{\ell=x,y} \sum_\sigma \varepsilon_p p_{a\ell\sigma}^\dagger p_{a\ell\sigma} \\ & + \sum_{\langle i,a \rangle} \sum_{\ell=x,y} \sum_\sigma t_{dp} (p_{a\ell\sigma}^\dagger d_{i\sigma} + d_{i\sigma}^\dagger p_{a\ell\sigma}) \\ & + \sum_{\langle a,b \rangle} \sum_\sigma t_{pp} (p_{a\ell\sigma}^\dagger p_{b\ell\sigma} + p_{b\ell\sigma}^\dagger p_{a\ell\sigma}), \end{aligned} \quad (4)$$

$$H' = \frac{1}{2} \sum_i \sum_{\sigma \neq \sigma'} U n_{di\sigma} n_{di\sigma'}. \quad (5)$$

Here $d_{i\sigma}$ and $p_{a\ell\sigma}$ ($d_{i\sigma}^\dagger$ and $p_{a\ell\sigma}^\dagger$) are the annihilation (creation) operators for the $\text{Cu}3d_{x^2-y^2}$ and $\text{O}2p_\ell$ electrons with spin σ , where the $\text{Cu}3d_{x^2-y^2}$ and $\text{O}2p_\ell$ orbitals form a σ -bond. $n_{di\sigma}$ is the number operator for the $3d_{x^2-y^2}$ electrons with spin σ at Cu site i . Summation with $\langle i, a \rangle$ ($\langle a, b \rangle$) is over nearest-neighbor Cu-O (O-O) bonds. We take $t_{dp} = 1.3$ eV, $t_{pp} = 0.65$ eV³⁶, and $U = 11$ eV as

in our previous work¹³. For the $1s$ electrons, we assume completely localized orbitals at each Cu site:

$$H_s = \sum_i \sum_\sigma \varepsilon_{1s} s_{i\sigma}^\dagger s_{i\sigma} = \sum_{\mathbf{k}} \sum_\sigma \varepsilon_{1s} s_{\mathbf{k}\sigma}^\dagger s_{\mathbf{k}\sigma}, \quad (6)$$

where ε_{1s} is the one-particle energy, $s_{i\sigma}$ ($s_{i\sigma}^\dagger$) is the annihilation (creation) operator for the $1s$ electrons with spin σ at Cu site i . $s_{\mathbf{k}\sigma}$ ($s_{\mathbf{k}\sigma}^\dagger$) is the momentum representation of $s_{i\sigma}$ ($s_{i\sigma}^\dagger$). H_{sd} is the Hund's rule coupling between the $1s$ and $3d$ electrons:

$$\begin{aligned} H_{sd} = & J_{sd} \sum_i \sum_{\sigma\sigma'} s_{i\sigma}^\dagger d_{i\sigma'}^\dagger s_{i\sigma'} d_{i\sigma} \\ = & -J_{sd} \sum_i [n_{si} n_{di} + \mathbf{s}_{si} \cdot \mathbf{s}_{di}], \end{aligned} \quad (7)$$

where n_{di} and \mathbf{s}_{di} (n_{si} and \mathbf{s}_{si}) are the number and spin-density operators for the $3d_{x^2-y^2}$ ($1s$) electron with spin σ at Cu site i , respectively. H_{sd} plays an essential role in our microscopic mechanism of two-magnon RIXS, which we shall below refer to as the Hund's coupling mechanism. H_p describes the conduction $4p$ band electrons:

$$H_p = \sum_{\mathbf{k}} \sum_\mu \sum_\sigma \varepsilon_{4p\mu}(\mathbf{k}) p_{\mathbf{k}\mu\sigma}'^\dagger p_{\mathbf{k}\mu\sigma}', \quad (8)$$

where $p_{\mathbf{k}\mu\sigma}'$ ($p_{\mathbf{k}\mu\sigma}'^\dagger$) is the annihilation (creation) operator of the $4p_\mu$ electron ($\mu = x, y, z$) with momentum \mathbf{k} and spin σ . H_x describes resonant $1s$ - $4p$ electric-dipole transition induced by x-rays:

$$H_x = \sum_{\mathbf{k}, \mathbf{q}} \sum_\mu \sum_\sigma w_\mu(\mathbf{q}, \mathbf{e}) \alpha_{\mathbf{q}\mathbf{e}} p_{\mathbf{k}+\mathbf{q}\mu\sigma}'^\dagger s_{\mathbf{k}\sigma} + h.c., \quad (9)$$

where $\alpha_{\mathbf{q}\mathbf{e}}$ is the annihilation operator of a photon with momentum \mathbf{q} and polarization \mathbf{e} . The electric-dipole transition matrix $w_\mu(\mathbf{q}, \mathbf{e})$ is given by

$$w_\mu(\mathbf{q}, \mathbf{e}) = -\frac{e}{m} \sqrt{\frac{2\pi}{|\mathbf{q}|}} \mathbf{e} \cdot \langle 4p_\mu | \mathbf{p} | 1s \rangle \propto \mathbf{e} \cdot \mathbf{e}_\mu, \quad (10)$$

in natural units ($c = \hbar = 1$), where \mathbf{e}_μ 's are the orthonormal basis vectors.

The microscopic mechanism of two-magnon excitations which we propose is schematically displayed in Fig. 1, where J_{sd} is the Hund's exchange integral included in the Hamiltonian H_{sd} . Each of two magnons is generated when the d -electron spin is flipped by J_{sd} at the excited site. The second spin flipping occurs at the same Cu site as the first one, but follows the first one with a delay shorter than the core-hole life time of the order of femtoseconds. J_{sd} is given by using the Slater-Condon integrals as $J_{sd} = G^2(s, d)/5 = G_2(s, d)^{37}$, and should be smaller than the core-hole Coulomb potential $F_2(s, d)$. Since the $3d$ and inner-shell $1s$ orbitals are both strongly localized, the core-hole potential $F_2(s, d)$ is usually chosen to be comparable to the $\text{Cu}3d$ Coulomb interaction U for La_2CuO_4 . Assuming that J_{sd} is one-order

smaller than the core-hole potential, we expect J_{sd} is of the order of 1 eV. Hereafter we refer to this mechanism as the Hund's coupling mechanism or the on-site exchange mechanism, to contrast with the inter-site exchange mechanism.

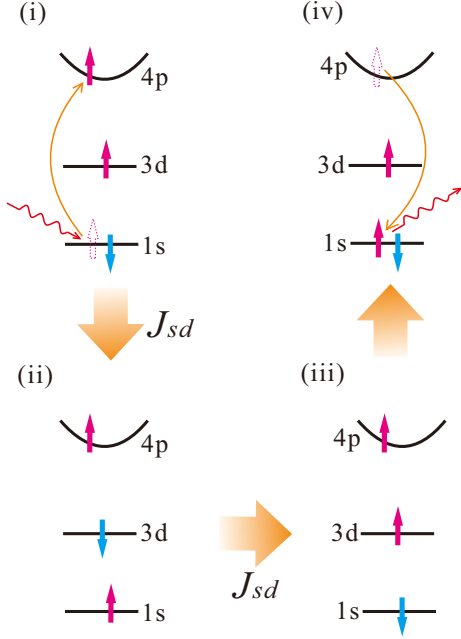


FIG. 1. (Color online) Schematic picture of two-magnon excitation in the Hund's coupling mechanism. (i) Incident x-ray resonantly promotes an inner-shell 1s electron to a conduction 4p band at a Cu site. (ii) The lone 1s core-level electron can exchange spins with the Cu 3d electron by means of the Hund's coupling J_{sd} . (iii) To second-order in J_{sd} , the spin state of the 1s and 3d electrons at the excited site can be recovered through another exchange process. Note that both the spin-flipping processes in (ii) and (iii) occur at the same excited site, since the 1s state is completely localized. (iv) Finally, the 4p electron excited in (i) goes back to the 1s core level, with emitting an x-ray. In the present figure, only 1s electron with up spin is promoted to a 4p band. Promotion of a 1s electron with down spin is also possible.

B. Two-magnon RIXS formula

Nozières and Abrahams (NA) developed a theoretical framework of electron Raman scattering by means of Keldysh perturbation theory, and discussed the threshold singularity in metals³⁸. Extending the NA's framework, we derived a formula for RIXS intensity at the transition-metal K edge^{12–14}, and thereby we explained experimental observations on charge-transfer and orbital excitations in K -edge RIXS for several transition-metal compounds^{39–41}. To calculate two-magnon RIXS spectra, we further extend our previous framework by a way different from Ref. 20, based on the Hund's coupling mechanism.

We adopt the SDW mean-field approach to describe the antiferromagnetic (AF) ground state^{42,43}. Within the SDW mean-field formalism, the Coulomb interaction part H' is approximated by

$$H'_{MF} = \frac{U}{2} \sum_{\mathbf{k}} \sum_{\sigma_1 \sigma_2} d_{\mathbf{k}\sigma_1\sigma_1}^\dagger [n_d \delta_{\sigma_1\sigma_2} - \mathbf{m} \cdot \boldsymbol{\sigma}_{\sigma_1\sigma_2}] d_{\mathbf{k}\sigma_2\sigma_2} - \frac{NU}{4} [n_d^2 - |\mathbf{m}|^2], \quad (11)$$

where \mathbf{k}_σ is defined as $\mathbf{k}_\uparrow = \mathbf{k}$ and $\mathbf{k}_\downarrow = \mathbf{k} + \mathbf{q}_{AF}$ with \mathbf{q}_{AF} the magnetic-ordering vector. n_d and \mathbf{m} are the mean-fields for the d -electron number and spin moment to be determined self-consistently, and $\boldsymbol{\sigma}$ is the Pauli matrix vector. In our calculation, we set the z -axis of spin along the crystallographic [001] (i.e., the c -axis) direction, and assume the commensurate AF ground state with $\mathbf{q}_{AF} = (\pi, \pi)$ and $\mathbf{m} \parallel [110]$ as observed in neutron scattering⁴⁴. Introducing new fermion annihilation and creation operators, the mean-field Hamiltonian $H_{d,MF} \equiv H_0 + H'_{MF}$ is diagonalized as:

$$H_{d,MF} = \sum_{\mathbf{k}} \sum_j E_j(\mathbf{k}) a_{j\mathbf{k}}^\dagger a_{j\mathbf{k}}, \quad (12)$$

where j is band index. $E_j(\mathbf{k})$ is the diagonalized band energy which the chemical potential is already subtracted from. The chemical potential is always determined so that the total electron number equals five per unit cell. The original d -electron annihilation and creation operators in the momentum representation are related to $a_{j\mathbf{k}}$ and $a_{j\mathbf{k}}^\dagger$ by

$$d_{\mathbf{k}\sigma\sigma} = \sum_j u_{\sigma,j}(\mathbf{k}_\sigma) a_{j\mathbf{k}}, \quad (13)$$

$$d_{\mathbf{k}\sigma\sigma}^\dagger = \sum_j u_{\sigma,j}^*(\mathbf{k}_\sigma) a_{j\mathbf{k}}^\dagger, \quad (14)$$

where $u_{\sigma,j}(\mathbf{k}_\sigma)$'s are the d -electron elements of the diagonalization matrix. The d -electron Green's function has a 2×2 matrix form:

$$\hat{G}(\mathbf{k}; \xi) = \begin{bmatrix} G_{\uparrow\uparrow}(\mathbf{k}_\uparrow, \mathbf{k}_\uparrow; \xi) & G_{\uparrow\downarrow}(\mathbf{k}_\uparrow, \mathbf{k}_\downarrow; \xi) \\ G_{\downarrow\uparrow}(\mathbf{k}_\downarrow, \mathbf{k}_\uparrow; \xi) & G_{\downarrow\downarrow}(\mathbf{k}_\downarrow, \mathbf{k}_\downarrow; \xi) \end{bmatrix}. \quad (15)$$

Each element of $\hat{G}(\mathbf{k}; \xi)$ is expressed as

$$G_{\sigma_1\sigma_2}(\mathbf{k}_{\sigma_1}, \mathbf{k}_{\sigma_2}; \xi) = \sum_j u_{\sigma_1,j}(\mathbf{k}_{\sigma_1}) u_{\sigma_2,j}^*(\mathbf{k}_{\sigma_2}) G_j(\mathbf{k}, \xi), \quad (16)$$

with

$$G_j(\mathbf{k}, \xi) = \frac{1}{\xi - E_j(\mathbf{k})}. \quad (17)$$

In our representation, the self-consistency equations for

n_d and \mathbf{m} become

$$n_d = -\sum_j \frac{1}{N} \sum_{\mathbf{k}} \sum_{\sigma_1 \sigma_2} \int_{-\infty}^{\infty} \frac{d\xi}{\pi} u_{\sigma_1, j}^*(\mathbf{k}_{\sigma_1}) \delta_{\sigma_1 \sigma_2} u_{\sigma_2, j}(\mathbf{k}_{\sigma_2}) \times f(\xi) \text{Im}[G_j^R(\mathbf{k}, \xi)], \quad (18)$$

$$\mathbf{m} = -\sum_j \frac{1}{N} \sum_{\mathbf{k}} \sum_{\sigma_1 \sigma_2} \int_{-\infty}^{\infty} \frac{d\xi}{\pi} u_{\sigma_1, j}^*(\mathbf{k}_{\sigma_1}) \sigma_{\sigma_1 \sigma_2} u_{\sigma_2, j}(\mathbf{k}_{\sigma_2}) \times f(\xi) \text{Im}[G_j^R(\mathbf{k}, \xi)], \quad (19)$$

where $f(\xi) = [1 + e^{\xi/T}]^{-1}$ is the Fermi distribution function at temperature T , $G_j^R(\mathbf{k}, z)$ is the retarded electron Green's function given by

$$G_j^R(\mathbf{k}, \xi) \equiv G_j(\mathbf{k}, \xi + i\gamma) = \frac{1}{\xi - E_j(\mathbf{k}) + i\gamma}, \quad (20)$$

with γ a small positive. Throughout our study, numerical integration in energy and momentum is carried out by discretizing the interval $-40 \text{ eV} < \xi < 40 \text{ eV}$ into 16000 energy points and the first Brillouin zone into $N = 80 \times 80$ \mathbf{k} points. We take $\gamma = 0.16 \text{ eV}$. We choose $\varepsilon_d - \varepsilon_p$ so that $\varepsilon_d - \varepsilon_p + Un_d/2 = 1.4 \text{ eV}$ for the non-magnetic state. The calculated spin moment and charge-transfer gap (insulating gap) are $|\mathbf{m}| = 0.61\mu_B$ and 2.55 eV .

To describe the electron dynamics in RIXS, we define the dynamical correlation function by

$$\Pi_{\sigma'_1 \sigma'_2, \sigma_2 \sigma_1}(\mathbf{q}, t' - t) = \langle \rho_{\sigma'_1 \sigma'_2}(\mathbf{q}, t') \rho_{\sigma_2 \sigma_1}(-\mathbf{q}, t) \rangle, \quad (21)$$

where $\rho_{\sigma_1 \sigma_2}(\mathbf{q}, t)$ is the density operator in the Heisenberg representation:

$$\rho_{\sigma_1 \sigma_2}(\mathbf{q}, t) = e^{iH_d t} \rho_{\sigma_1 \sigma_2}(\mathbf{q}) e^{-iH_d t}, \quad (22)$$

$$\rho_{\sigma_1 \sigma_2}(\mathbf{q}) = \sum_{\mathbf{k}} d_{\mathbf{k}_{\sigma_1} \sigma_1}^\dagger d_{\mathbf{k}_{\sigma_2} + \mathbf{q}, \sigma_2}. \quad (23)$$

Fourier transform of the dynamical correlation function is related to the linear-response susceptibility in terms of the fluctuation-dissipation theorem:

$$\Pi_{\sigma'_1 \sigma'_2, \sigma_2 \sigma_1}(\mathbf{q}, \omega) = \frac{\chi_{\sigma'_1 \sigma'_2, \sigma_2 \sigma_1}^R(\mathbf{q}, \omega) - \chi_{\sigma'_1 \sigma'_2, \sigma_2 \sigma_1}^A(\mathbf{q}, \omega)}{i(1 - e^{-\omega/T})}, \quad (24)$$

where $\chi_{\sigma'_1 \sigma'_2, \sigma_2 \sigma_1}^{R(A)}(\mathbf{q}, \omega)$ is the retarded (advanced) branch of the susceptibility:

$$\chi_{\sigma'_1 \sigma'_2, \sigma_2 \sigma_1}^R(\mathbf{q}, \omega) = \chi_{\sigma'_1 \sigma'_2, \sigma_2 \sigma_1}(\mathbf{q}, \omega + i\gamma), \quad (25)$$

$$\chi_{\sigma'_1 \sigma'_2, \sigma_2 \sigma_1}^A(\mathbf{q}, \omega) = \chi_{\sigma'_1 \sigma'_2, \sigma_2 \sigma_1}(\mathbf{q}, \omega - i\gamma). \quad (26)$$

$\chi_{\sigma'_1 \sigma'_2, \sigma_2 \sigma_1}(\mathbf{q}, \omega)$ is the Fourier transform of

$$\chi_{\sigma'_1 \sigma'_2, \sigma_2 \sigma_1}(\mathbf{q}, t' - t) = i \langle T[\rho_{\sigma'_1 \sigma'_2}(\mathbf{q}, t') \rho_{\sigma_2 \sigma_1}(-\mathbf{q}, t)] \rangle, \quad (27)$$

where $T[\dots]$ means the ordinary time-ordered product. We calculate $\chi_{\sigma'_1 \sigma'_2, \sigma_3 \sigma_4}^{R, A}(\mathbf{q}, \omega)$ within the random-phase approximation (RPA):

$$\chi_{\sigma_1 \sigma_2, \sigma_3 \sigma_4}^{R, A}(\mathbf{q}, \omega) = \chi_{\sigma_1 \sigma_2, \sigma_3 \sigma_4}^{(0) R, A}(\mathbf{q}, \omega) - \sum_{\sigma'_1 \dots \sigma'_4} \chi_{\sigma_1 \sigma_2, \sigma'_3 \sigma'_4}^{(0) R, A}(\mathbf{q}, \omega) \Gamma_{\sigma'_3 \sigma'_1, \sigma'_2 \sigma'_4}^{(0)} \chi_{\sigma'_1 \sigma'_2, \sigma_3 \sigma_4}^{R, A}(\mathbf{q}, \omega) \quad (28)$$

where

$$\Gamma_{\sigma'_3 \sigma'_1, \sigma'_2 \sigma'_4}^{(0)} = U(\delta_{\sigma'_1 \sigma'_2} \delta_{\sigma'_3 \sigma'_4} - \delta_{\sigma'_1 \sigma'_2} \delta_{\sigma'_3 \sigma'_4}) \quad (29)$$

is the Coulomb interaction at Cu site. $\chi_{\sigma_1 \sigma_2, \sigma_3 \sigma_4}^{(0)}(\mathbf{q}, \omega)$ is the bare susceptibility calculated by

$$\begin{aligned} \chi_{\sigma_1 \sigma_2, \sigma_3 \sigma_4}^{(0) R}(\mathbf{q}, \omega) &= \frac{1}{N} \sum_{\mathbf{k}} \int_{-\infty}^{\infty} \frac{d\xi}{\pi} \sum_{j, j'} u_{\sigma_4, j}(\mathbf{k}_{\sigma_4}) u_{\sigma_1, j}^*(\mathbf{k}_{\sigma_1}) u_{\sigma_2, j'}(\mathbf{k}_{\sigma_2} + \mathbf{q}) u_{\sigma_3, j'}^*(\mathbf{k}_{\sigma_3} + \mathbf{q}) \\ &\quad \times \{f(\xi) \text{Im}[G_j^R(\mathbf{k}, \xi)] G_{j'}^R(\mathbf{k} + \mathbf{q}, \xi + \omega) + f(\xi + \omega) G_j^A(\mathbf{k}, \xi) \text{Im}[G_{j'}^R(\mathbf{k} + \mathbf{q}, \xi + \omega)]\} \quad (30) \\ \chi_{\sigma_1 \sigma_2, \sigma_3 \sigma_4}^{(0) A}(\mathbf{q}, \omega) &= -\frac{1}{N} \sum_{\mathbf{k}} \int_{-\infty}^{\infty} \frac{d\xi}{\pi} \sum_{j, j'} u_{\sigma_4, j}(\mathbf{k}_{\sigma_4}) u_{\sigma_1, j}^*(\mathbf{k}_{\sigma_1}) u_{\sigma_2, j'}(\mathbf{k}_{\sigma_2} + \mathbf{q}) u_{\sigma_3, j'}^*(\mathbf{k}_{\sigma_3} + \mathbf{q}) \\ &\quad \times \{f(\xi) \text{Im}[G_j^A(\mathbf{k}, \xi)] G_{j'}^A(\mathbf{k} + \mathbf{q}, \xi + \omega) + f(\xi + \omega) G_j^R(\mathbf{k}, \xi) \text{Im}[G_{j'}^A(\mathbf{k} + \mathbf{q}, \xi + \omega)]\} \quad (31) \end{aligned}$$

where $G_j^A(\mathbf{k}, \xi) = G_j^{R*}(\mathbf{k}, \xi)$. Energy-momentum summation in Eqs. (30) and (31) is numerically performed using fast Fourier transformation (FFT). Diagrammatic representation of RPA is presented in Fig. 2(a).

The single-magnon spectrum to be observed in neutron scattering is given by the dynamical spin correlation function:

$$S_{+-}(\mathbf{q}, \omega) = \sum_{\sigma_1 - 4} ' [\sigma_+]_{\sigma_1 \sigma_2} [\sigma_-]_{\sigma_3 \sigma_4} \Pi_{\sigma_1 \sigma_2, \sigma_3 \sigma_4}(\mathbf{q} + \mathbf{q}_{\sigma_1 \sigma_2}, \omega), \quad (32)$$

where $\sigma_{\pm} = (\sigma_x \pm i\sigma_y)/2$ using the Pauli matrices, and $\mathbf{q}_{\sigma_1 \sigma_2} = \mathbf{k}_{\sigma_1} - \mathbf{k}_{\sigma_2}$. Summation in spin is restricted to the cases when $\mathbf{q}_{\sigma_1 \sigma_2} - \mathbf{q}_{\sigma_4 \sigma_3}$ is equivalent to the Γ point.

RIXS intensity from two-magnon excitations can be calculated in a similar way to that in Ref. 13 by means of the Keldysh diagrammatic technique³⁸. In the Keldysh diagrammatic representation, probability of excitations where a pair of magnons are left in the final state is expressed by the diagrams where a pair of magnon propagators bridge the upper normally and lower reversely time-ordered branches. As shown in Fig. 2(b), corresponding to two ways of contraction, RIXS intensity from two-magnon excitations consists of two contributions:

$$W(q\mathbf{e}; q'\mathbf{e}') = W_p(q\mathbf{e}; q'\mathbf{e}') + W_c(q\mathbf{e}; q'\mathbf{e}'), \quad (33)$$

where the left [right] diagram including a parallel [crossed] pair of magnon propagators expresses $W_p(q\mathbf{e}; q'\mathbf{e}')$ [$W_c(q\mathbf{e}; q'\mathbf{e}')$]. Those terms are analytically expressed as the convolution of the dynamical correlation function:

$$W_p(q\mathbf{e}; q'\mathbf{e}') = \sum_{\sigma_1\sigma_2} \sum_{\sigma'_1\sigma'_2} \frac{1}{N} \sum_{\mathbf{p}} \int_{-\infty}^{\infty} \frac{d\xi}{2\pi} \Pi_{\sigma'_1\sigma'_2, \sigma_2\sigma_1}(\mathbf{p}, \xi) \Pi_{\sigma'_2\sigma'_1, \sigma_1\sigma_2}(\mathbf{Q} - \mathbf{p}, \Omega - \xi) |R(q, q'; \xi)|^2, \quad (34)$$

$$W_c(q\mathbf{e}; q'\mathbf{e}') = \sum_{\sigma_1\sigma_2} \sum_{\sigma'_1\sigma'_2} \frac{1}{N} \sum_{\mathbf{p}} \int_{-\infty}^{\infty} \frac{d\xi}{2\pi} \Pi_{\sigma'_1\sigma'_2, \sigma_2\sigma_1}(\mathbf{p}, \xi) \Pi_{\sigma'_2\sigma'_1, \sigma_1\sigma_2}(\mathbf{Q} - \mathbf{p}, \Omega - \xi) R(q, q'; \xi) R^*(q, q'; \Omega - \xi), \quad (35)$$

where $q = (\mathbf{q}, \omega)$ and $\mathbf{e} [q' = (\mathbf{q}', \omega')]$ and \mathbf{e}' are the four-momentum and polarization of the absorbed [emitted] x-ray, $\mathbf{Q} \equiv \mathbf{q} - \mathbf{q}'$ and $\Omega \equiv \omega - \omega'$ are the momentum transfer and energy loss of x-rays. $R(q, q'; \xi)$ is the resonance factor given by

$$R(q, q'; \xi) = J_{sd}^2 \sum_{\mu=x,y,z} \frac{1}{N} \sum_{\mathbf{k}} \frac{w_{\mu}(\mathbf{q}, \mathbf{e}) w_{\mu}^*(\mathbf{q}', \mathbf{e}')}{\Delta_{\mu}(\mathbf{k}) [\Delta_{\mu}(\mathbf{k}) - \xi] \Delta'_{\mu}(\mathbf{k})}, \quad (36)$$

with

$$\begin{aligned} \Delta_{\mu}(\mathbf{k}) &= \omega + \varepsilon_{1s} + i\Gamma_{1s} - \varepsilon_{4p\mu}(\mathbf{k}) \\ &\equiv \tilde{\Delta} - \varepsilon_{4p\mu}(\mathbf{k}) \end{aligned} \quad (37)$$

$$\begin{aligned} \Delta'_{\mu}(\mathbf{k}) &= \omega' + \varepsilon_{1s} + i\Gamma_{1s} - \varepsilon_{4p\mu}(\mathbf{k}) \\ &= \tilde{\Delta} - \varepsilon_{4p\mu}(\mathbf{k}) - \Omega. \end{aligned} \quad (38)$$

In terms of the density of states (DOS) of the $4p_{\mu}$ band,

$$\rho_{4p\mu}(\varepsilon) = \frac{1}{N} \sum_{\mathbf{k}} \delta(\varepsilon - \varepsilon_{4p\mu}(\mathbf{k})), \quad (39)$$

the resonance factor is written as

$$R(q, q'; \xi) = J_{sd}^2 \sum_{\mu} \int_{E_F}^{\infty} d\varepsilon \frac{w_{\mu}(\mathbf{q}, \mathbf{e}) w_{\mu}^*(\mathbf{q}', \mathbf{e}') \rho_{4p\mu}(\varepsilon)}{(\tilde{\Delta} - \varepsilon)(\tilde{\Delta} - \varepsilon - \xi)(\tilde{\Delta} - \varepsilon - \Omega)}. \quad (40)$$

For the below numerical calculations for RIXS spectra, we use $\rho_{4p\mu}(\varepsilon)$ obtained from a first-principles band calculation and $\varepsilon_{1s} = -8980$ eV, which reproduce well experimental x-ray absorption spectra (XAS) as shown in the Appendix.

III. NUMERICAL RESULTS

A. Single-magnon excitations

Consistency between calculated single-magnon spectra and neutron scattering data is prerequisite for calculation of two-magnon RIXS spectra. The numerical results for the dynamical spin correlation function $S_{+-}(\mathbf{q}, \omega)$ are displayed in Fig. 3. As shown in Ref. 43, the SDW approach yields the spin-wave (i.e., single-magnon) dispersion precisely agreeing with neutron scattering. Although we use the d - p model which includes the O- $2p$ orbitals and differs from the simple Hubbard model in Ref. 43, the dispersion is well reproduced again to agree with neutron scattering data. It is known that SW calculation in the simple nearest-neighbor Heisenberg model

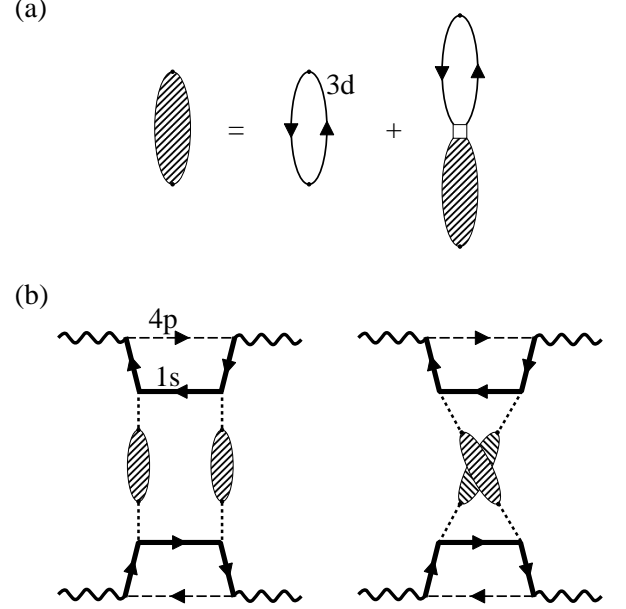


FIG. 2. (a) Summation of diagrams for RPA. Shaded oval and oriented solid lines represent the RPA susceptibility (i.e., the single-magnon propagator) and the Green's function for the 3d electrons, respectively. The empty square represents the 3d Coulomb interaction matrix $\Gamma^{(0)}$. (b) Two contributions from two-magnon excitations to RIXS spectra. Wavy lines, oriented thick solid and oriented thin broken lines represent propagation of x-rays, 1s and 4p electrons, respectively. Dotted lines denote the on-site Hund's rule coupling J_{sd} between the 1s and 3d electrons at each Cu site.

leads to $\omega(\pi, 0) = \omega(\pi/2, \pi/2)$, being inconsistent with neutron scattering. An advantage of the SDW formalism is that the magnon excitation energies are correctly reproduced at those \mathbf{q} points. One of notable features is that the strong divergent behavior around $\mathbf{q} = (\pi, \pi)$. This divergent behavior is observed in neutron scattering⁴⁵, which becomes important for the two-magnon RIXS intensities around the zone center, as we shall see below.

B. Dependence on x-ray momentum transfer

Calculated two-magnon RIXS spectra are compared with experimental ones at various momentum transfers in Fig. 4. In Fig. 4(e), vanishing of the two-magnon RIXS spectrum at $\mathbf{Q} = (\pi, \pi)$ is reproduced, being consistent with experiments and also with other previous theoretical

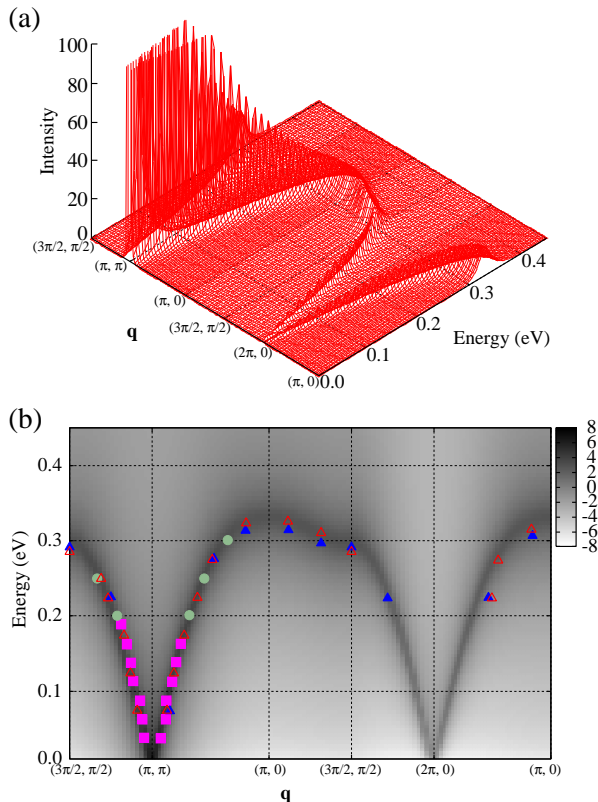


FIG. 3. (Color online) Calculated dynamical spin correlation function $S_{+-}(\mathbf{q}, \omega)$ along symmetry lines. Vertical axis in (a) represents calculated intensity in a linear scale, while the gray-level scale in (b) represents in a logarithmic scale. In (b), plots are neutron-scattering data read from Ref. 45: $T = 10$ K (empty symbols) and 295 K (filled symbols). Squares are obtained for $E_i = 250$ meV, circles for $E_i = 600$ meV, and triangles for $E_i = 750$ meV, where E_i is incident neutron energy⁴⁵.

calculations. In Fig. 4(a), the monotonic slope below 0.65 eV is responsible for disagreement between the calculated curve and the experimental plots. We speculate that this slope may be subtracted together with the elastic line in experiments. Considering uncertainty due to elastic-line subtraction and limited resolution in the experiment, we regard the theoretical curves as agree well with the experimental plots.

To see more detailed momentum dependence of the two-magnon RIXS spectrum, we present the intensity along symmetry lines in the first Brillouin zone in Fig. 5(a). A notable feature is that the intensity gets stronger toward $\mathbf{Q} = 0$ and $\Omega = 0$, which has not been pointed out in previous experiments and theoretical calculations. This notable feature is straightforwardly understood in the following way: Intensity of single-magnon excitations becomes divergent toward $\mathbf{q} = (\pi, \pi)$ as observed in neutron scattering and also as calculated in III A. Therefore, excitation of two magnons with $\mathbf{p}_1, \mathbf{p}_2 \approx (\pi, \pi)$ contributes strongly to the two-magnon spectrum around $\mathbf{Q} = \mathbf{p}_1 + \mathbf{p}_2 \approx (2\pi, 2\pi) \equiv (0, 0)$. This is a

striking difference from the previous two-magnon RIXS calculations. The difference arises from the difference in starting models, rather than from that in the underlying microscopic mechanisms. As shown in Ref. 21, the magnetic scattering operator involving two spins is proportional to or commutable with the starting Heisenberg spin Hamiltonian at $\mathbf{Q} = 0$, and therefore can never excite the ground eigenstate to any other states. This peculiarity of Heisenberg spin models leads to the vanishing of RIXS intensity at $\mathbf{Q} = 0$. On the other hand, such vanishing does not occur in Hubbard-type Hamiltonians.

In Fig. 5(b), we compare the calculated intensity map with experimental peak positions. Although the calculated intensity map shows broadness of spectra, the experimental peak positions fall well within an energy-loss range where the calculated intensity is relatively strong, except for $\mathbf{Q} = (\pi, \pi)$. In Fig. 5(c), we compare the integrated weights between the calculation and experiment. In calculation, we have integrated $W(\mathbf{q}\mathbf{e}; \mathbf{q}'\mathbf{e}')$ in energy loss Ω up to 1 eV. Integration of the intensity yields a large integrated weight near the zone center, which contradicts the vanishing weight concluded in previous theoretical and experimental works. In Heisenberg spin models, the intensity vanishes at the zone center and therefore also the integrated weight vanishes there, unless ring spin exchange is taken into account^{20,21,24}. As we pointed out already, this vanishing arises from the peculiarity of Heisenberg spin models. In experiment, the RIXS intensity around the zone center is overlaid by the much stronger elastic line, and is difficult to distinguish from it. In the experiment of Ref. 19, the two-magnon RIXS weight is postulated to be zero at the zone center. However, supposing that two-magnon RIXS intensity may be subtracted together with the elastic line in analyzing experimental data, still one cannot exclude the possibility that the two-magnon RIXS weight takes a finite value at the zone center.

In Fig. 5(c), the calculated weight at $\mathbf{Q} = (\pi, \pi)$ seems finite, which will be inaccurate due to the limited precision of numerical integration. One may expect that the weight approaches zero more closely, if we take smaller γ and finer energy-momentum discretization for numerical integration.

C. Dependence on incident x-ray energy and polarization

In experiments^{18,19}, the two-magnon RIXS weight was not observed for the polarization geometry $E \parallel ab$. To explain this, we calculate the dependence of two-magnon RIXS spectra on x-ray polarization direction, whose results are shown in Fig. 6. According to the calculated results, the two-magnon RIXS intensity for $E \parallel ab$ will be enhanced at higher incident x-ray energies (by about 4 eV) than that for $E \parallel c$. However, the intensity for $E \parallel ab$ is much weaker even at the resonance than for $E \parallel c$, which explains the missing of this feature in exper-

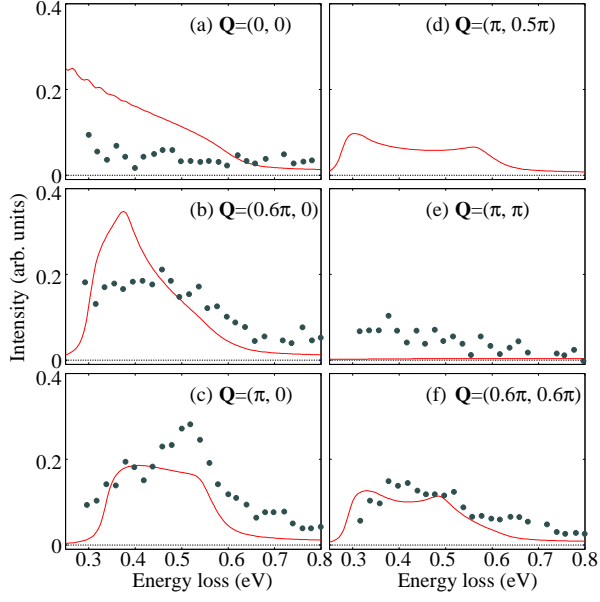


FIG. 4. (Color online) Comparison with experimental data at various momentum transfers. Curves are the calculated results, and plots are experimental data read from Ref. 18. X-ray polarization direction is fixed to $E \parallel c$. Theoretical intensity is scaled to match the experimental plots, using a single scale factor common to all the panels.

iments. This weakness of the intensity for $E \parallel ab$ arises from the smallness of the resonance factor, and therefore, roughly speaking, can be attributed to the smallness and broadness of the $4p$ DOS $\rho_{4px,y}(\varepsilon)$. More careful investigation may confirm a small but finite two-magnon weight for $E \parallel ab$.

IV. DISCUSSION

We have introduced that a new microscopic mechanism based on the Hund's rule coupling between the Cu $1s$ and $3d$ electrons. Here we show that the RIXS intensity calculated on the Hund's-coupling mechanism is evaluated to be the same or even stronger than that on the inter-site exchange mechanism. In either case of the inter-site exchange mechanism and the Hund's-coupling mechanism, we calculate the convolution of the dynamical spin correlation function to obtain two-magnon RIXS spectra. Therefore difference in the magnitude of spectra arises from that in the resonance factor. According to Ref. 20, the resonance factor in the inter-site exchange mechanism is given by

$$L_B(q, q') = -J_c \sum_{\mu} \int_{E_F}^{\infty} d\varepsilon \frac{w_{\mu}(\mathbf{q}, \mathbf{e}) w_{\mu}(\mathbf{q}', \mathbf{e}') \rho_{4p\mu}(\varepsilon)}{(\tilde{\Delta} - \varepsilon)(\tilde{\Delta} - \varepsilon - \Omega)} \quad (41)$$

where J_c is the modification to the AF Heisenberg exchange J , and roughly evaluated as $J_c \sim 0.2 - 0.5$ eV²⁰ or $J_c \sim \eta J$ with $\eta \sim -0.8$ or 1.7 ²⁴. Comparing with $R(q, q'; \xi)$ of Eq. (40), relative magnitude of the spectra

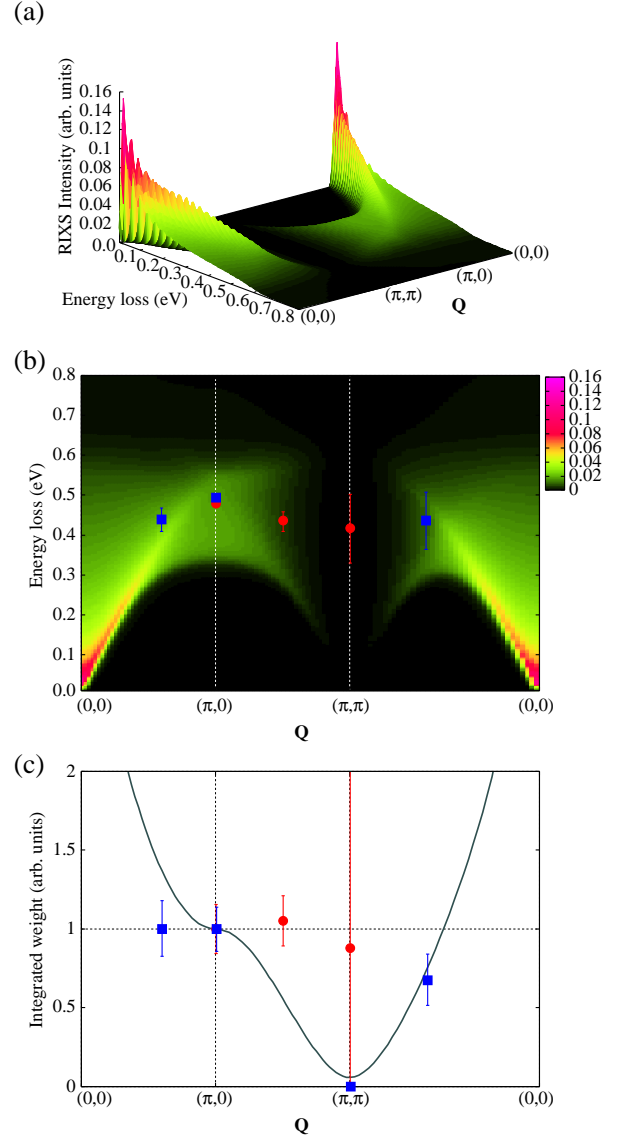


FIG. 5. (Color online) (a) Calculated RIXS intensity along symmetry lines. (b) Comparison with experimental peak positions and calculated intensity map along symmetry lines. (c) Comparison of integrated weight between calculation and experiment. Plots are read from Ref. 19. In (c), the weights are normalized by the value at $\mathbf{Q} = (\pi, 0)$. In Ref. 19, the integrated weight at $\mathbf{Q} = 0$ is postulated to be zero, whose plot is omitted here. X-ray polarization direction is always fixed to $E \parallel c$, and the incident x-ray energy for calculation is fixed to $\omega = 8992$ eV.

at the resonance, where $\omega + \varepsilon_{1s} - \bar{\varepsilon}_{4p} \approx 0$ with $\bar{\varepsilon}_{4p}$ a typical energy of the $4p$ states, is roughly evaluated by

$$\left| \frac{R(q, q'; \omega_{sm})}{L_B(q, q')} \right|^2 \sim \left| \frac{J_{sd}^2}{(\tilde{\Delta} - \bar{\varepsilon}_{4p} - \omega_{sm}) J_c} \right|^2 \sim \frac{J_{sd}^4}{[\omega_{sm}^2 + \Gamma_{1s}^2] J_c^2}, \quad (42)$$

where ω_{sm} is a typical energy of single-magnon excitation $\omega_{sm} \sim 300$ meV. If we set $J_{sd} = 1$ eV, $J_c = 0.5$ eV and $\Gamma_{1s} = 1$ eV, then $|R(q, q'; \omega_{sm})/L_B(q, q')|^2 \sim 4$. Thus we

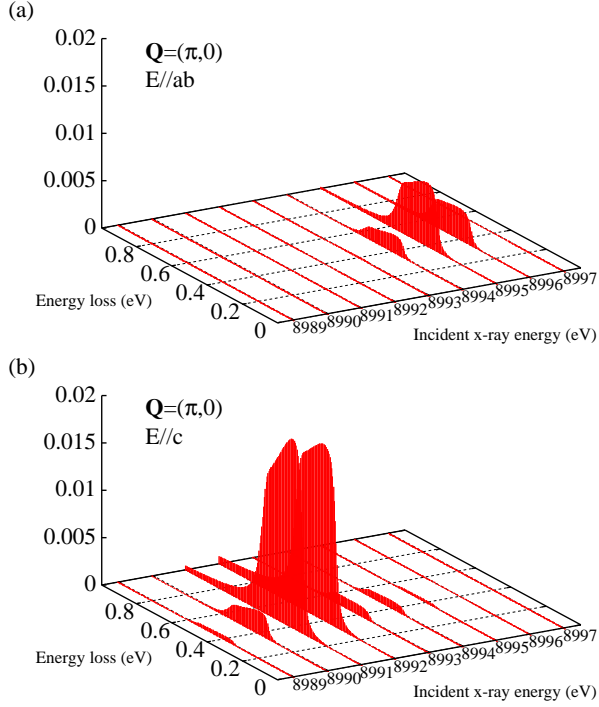


FIG. 6. (Color online) Incident x-ray energy dependence for two polarization directions (a) $E \parallel ab$ and (b) $E \parallel c$. X-ray momentum transfer is fixed to $\mathbf{Q} = (\pi, 0)$.

conclude that the Hund's coupling mechanism leads to the same or even larger magnitude of two-magnon RIXS spectra than the inter-site exchange mechanism.

As we explained already, the strong intensity around the zone center is not obtained from Heisenberg spin models. Furthermore, we point out that this strong intensity around the zone center cannot be captured by the FL framework on Raman light scattering. In the Hund's coupling mechanism of two-magnon RIXS, the scattering vertex function $R(q, q'; \xi)$ does not depend on the momenta of two excited magnons, as seen in Eqs. (34) and (35). This originates from the localized nature of spin flipping in the Hund's coupling mechanism. On the other hand, the FL Hamiltonian leads to a momentum dependent scattering vertex as a result from the nature of inter-site interactions, and fails to pick up the strong contribution from the two magnons $\mathbf{p}_1, \mathbf{p}_2 \approx (\pi, \pi)$. In fact, the dominant B_{1g} Raman spectrum is calculated by integrating a function including a factor $\sim \cos p_x - \cos p_y$ ^{34,35}, which makes the above two magnons $\mathbf{p}_1, \mathbf{p}_2$ much less important.

In our calculation, magnon-magnon interaction is not included. In our framework, magnon-magnon interactions are expressed by diagrams in which the two shaded ovals in Fig. 2(b) are connected by some diagrammatic elements. Unfortunately, magnon-magnon interactions are difficult to include into our calculation in some closed

form. However, if magnon-magnon interactions would be effective, then the two-magnon RIXS peak and weight should shift to lower energies, as seen in two-magnon light scattering. It is still unclear whether or not such a shift could yield better agreement with the experimental plots in the RIXS case. In Raman light scattering, characteristic spectral lineshapes confirmed the importance of magnon-magnon interactions²⁶⁻³⁰. Similarly, to get an insight into how important the magnon-magnon interactions are in RIXS, experimental data with higher resolution and clear spectral lineshape are needed.

V. CONCLUSION

We proposed a new microscopic mechanism of two-magnon RIXS, where the $1s-3d$ Hund's coupling induces a pair of magnons at each transition-metal site. Based on the new mechanism, we have calculated the two-magnon RIXS spectra at the K -edge, using an itinerant Hubbard-type Hamiltonian and the SDW mean-field formalism. Sharp contrast to previous studies based on Heisenberg spin models and the SW approximation is that the two-magnon excitations can take a sizable weight at the zone center. Careful experimental investigations around the zone center may enable us to get insights into whether our new microscopic mechanism is valid or not and how well such itinerant models describe two-magnon excitations compared with localized spin models.

ACKNOWLEDGMENTS

The author would like to thank Prof. J. Igarashi, Dr. K. Ishii and Prof. T. Nagao for invaluable communications.

Appendix A: X-ray absorption spectra

X-ray absorption spectra (XAS) at the $1s-4p$ resonance can be approximately calculated from the conduction $4p$ -band DOS $\rho_{4p\mu}(\varepsilon)$ with neglecting core-hole bound states:

$$A(q, \mathbf{e}) = -2 \sum_{\mu=x,y,z} |w_{\mu}(\mathbf{q}, \mathbf{e})|^2 \int_{E_F}^{\infty} \frac{d\varepsilon}{\pi} \text{Im} \left[\frac{\rho_{4p\mu}(\varepsilon)}{\tilde{\Delta} - \varepsilon} \right], \quad (\text{A1})$$

where $q = (\mathbf{q}, \omega)$, $\tilde{\Delta} = \omega + \varepsilon_{1s} + i\Gamma_{1s}$, and $\Gamma_{1s} = 1$ eV in our numerical calculation. We calculate $\rho_{4p\mu}(\varepsilon)$ using the WIEN2k code⁴⁶. In Fig. 7, calculated XAS spectra are compared with the experimental data read from Ref. 47 for two polarization directions $E \parallel ab$ and $E \parallel c$. For the both cases of polarization, the main peak positions agree well with the experimental ones by setting $\varepsilon_{1s} = -8980$ eV.

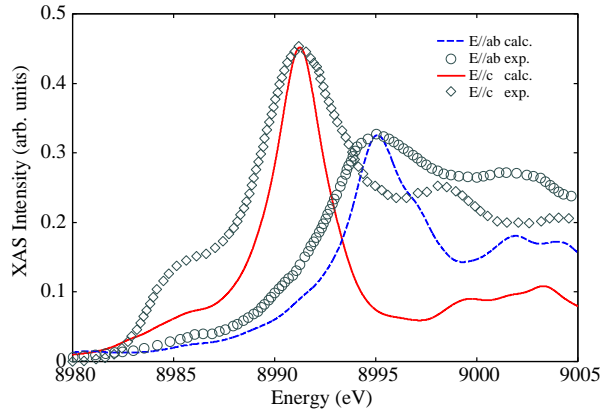


FIG. 7. (Color online) Resonant x-ray absorption spectra for $E \parallel ab$ and $E \parallel c$ geometries. Curves and plots are the theoretical and experimental data, respectively. The plots are read from Ref. 47. Experimental intensity is rescaled so that the peak intensity matches the calculated one.

-
- * nomurat@spring8.or.jp
- ¹ L.J.P. Ament, M. van Veenendaal, T.P. Devereaux, J.P. Hill, and J. van den Brink, *Rev. Mod. Phys.* **83**, 705 (2011).
 - ² K. Ishii, T. Tohyama, and J. Mizuki, *J. Phys. Soc. Jpn.* **82**, 021015 (2013).
 - ³ M.Z. Hasan, E.D. Isaacs, Z.X. Shen, L.L. Miller, K. Tsutsui, T. Tohyama and S. Maekawa, *Science* **288**, 1811 (2000).
 - ⁴ Y.J. Kim, J. P. Hill, C.A. Burns, S. Wakimoto, R.J. Birgeneau, D. Casa, T. Gog and C.T. Venkataraman, *Phys. Rev. Lett.* **89**, 177003 (2002).
 - ⁵ S. Suga, S. Imada, A. Higashiya, A. Shigemoto, S. Kasai, M. Sing, H. Fujiwara, A. Sekiyama, A. Yamasaki, C. Kim, T. Nomura, J. Igarashi, M. Yabashi and T. Ishikawa, *Phys. Rev. B* **72**, 081101(R) (2005).
 - ⁶ K. Ishii, S. Ishihara, Y. Murakami, K. Ikeuchi, K. Kuzushita, T. Inami, K. Ohkawa, M. Yoshida, I. Jarrige, N. Tatami, S. Nioka, D. Bizen, Y. Ando, J. Mizuki, S. Maekawa and Y. Endoh, *Phys. Rev. B* **83**, 241101(R) (2011).
 - ⁷ I. Jarrige, T. Nomura, K. Ishii, H. Gretarsson, Y.J. Kim, J. Kim, M. Upton, D. Casa, T. Gog, M. Ishikado, T. Fukuda, M. Yoshida, J.P. Hill, X. Liu, N. Hiraoka, K.D. Tsuei and S. Shamoto, *Phys. Rev. B* **86**, 115104 (2012).
 - ⁸ L. Braicovich, J. van den Brink, V. Bisogni, M. Moretti Sala, L.J.P. Ament, N.B. Brookes, G.M. De Luca, M. Saluzzo, T. Schmitt, V.N. Strocov, and G. Ghiringhelli, *Phys. Rev. Lett.* **104**, 077002 (2010).
 - ⁹ M. Guarise, B. Dalla Piazza, M. Moretti Sala, G. Ghiringhelli, L. Braicovich, H. Berger, J. N. Hancock, D. van der Marel, T. Schmitt, V. N. Strocov, L. J. P. Ament, J. van den Brink, P.-H. Lin, P. Xu, H. M. Rønnow, and M. Grioni, *Phys. Rev. Lett.* **105**, 157006 (2010).
 - ¹⁰ K. Tsutsui, T. Tohyama and S. Maekawa, *Phys. Rev. Lett.* **83**, 3705 (1999).
 - ¹¹ T. Ide and A. Kotani, *J. Phys. Soc. Jpn.* **69**, 3107 (2000).
 - ¹² T. Nomura and J. Igarashi, *J. Phys. Soc. Jpn.* **73**, 1677 (2004).
 - ¹³ T. Nomura and J. Igarashi, *Phys. Rev. B* **71**, 035110 (2005).
 - ¹⁴ J. Igarashi, T. Nomura and M. Takahashi, *Phys. Rev. B* **74**, 245122 (2006).
 - ¹⁵ J. van den Brink and M. van Veenendaal, *Europhys. Lett.* **73**, 121 (2006).
 - ¹⁶ L.J.P. Ament, F. Forte, and J. van den Brink, *Phys. Rev. B* **75**, 115118 (2007).
 - ¹⁷ N. Pakhira, J.K. Freericks and A.M. Shvaika, *Phys. Rev. B* **86**, 125103 (2012).
 - ¹⁸ J.P. Hill, G. Blumberg, Y.-J. Kim, D.S. Ellis, S. Wakimoto, R.J. Birgeneau, S. Komiya, Y. Ando, B. Liang, R.L. Greene, D. Casa, and T. Gog, *Phys. Rev. Lett.* **100**, 097001 (2008).
 - ¹⁹ D.S. Ellis, J. Kim, J.P. Hill, S. Wakimoto, R.J. Birgeneau, Y. Shvyd'ko, D. Casa, T. Gog, K. Ishii, K. Ikeuchi, A. Paramekanti, and Y.-J. Kim, *Phys. Rev. B* **81**, 085124 (2010).
 - ²⁰ T. Nagao and J. Igarashi, *Phys. Rev. B* **75**, 214414 (2007).
 - ²¹ J. van den Brink, *Europhys. Lett.* **80**, 47003 (2007).
 - ²² F.H. Vernay, M.J.P. Gingras, and T.P. Devereaux, *Phys. Rev. B*, **75**, 020403 (2007).
 - ²³ A. Donkov and A.V. Chubukov, *Phys. Rev. B*, **75**, 024417 (2007).
 - ²⁴ F. Forte, L.J.P. Ament, and J. van den Brink, *Phys. Rev. B* **77**, 134428 (2008).
 - ²⁵ P.A. Fleury and R. Loudon, *Phys. Rev.* **166**, 514 (1968).
 - ²⁶ R.J. Elliott, M.F. Thorpe, G.F. Imbusch, R. Loudon, and J.B. Parkinson, *Phys. Rev. Lett.* **21**, 147 (1968).
 - ²⁷ P.A. Fleury, *Phys. Rev. Lett.* **21**, 151 (1968).
 - ²⁸ R.J. Elliott and M.F. Thorpe, *J. Phys. C* **2**, 1630 (1969).
 - ²⁹ J.B. Parkinson, *J. Phys. C* **2**, 1012 (1969).
 - ³⁰ P.A. Fleury and H.J. Guggenheim, *Phys. Rev. Lett.* **24**, 1346 (1970).
 - ³¹ R.R.P. Singh, P.A. Fleury, K.B. Lyons, and P.E. Sulewski, *Phys. Rev. Lett.* **62**, 2736 (1989).
 - ³² B.S. Shastry and B.I. Shraiman, *Phys. Rev. Lett.* **65**, 1068 (1990).

- ³³ C.M. Canali and S.M. Girvin, Phys. Rev. B **45**, 7127 (1992).
- ³⁴ A.V. Chubukov and D.M. Frenkel, Phys. Rev. B **52**, 9760 (1995).
- ³⁵ A.W. Sandvik, S. Capponi, D. Poilblanc and E. Dagotto, Phys. Rev. B **57**, 8478 (1998).
- ³⁶ M. S. Hybertsen and M. Schlüter, Phys. Rev. B **39**, 9028 (1989).
- ³⁷ E.U. Condon and G.H. Shortley, *The Theory of Atomic Spectra* (Cambridge University Press, Cambridge, 1959).
- ³⁸ P. Nozières and E. Abrahams, Phys. Rev. B **10**, 3099 (1974).
- ³⁹ M. Takahashi, J. Igarashi and T. Nomura, Phys. Rev. B **75**, 235113 (2007).
- ⁴⁰ T. Semba, M. Takahashi and J. Igarashi, Phys. Rev. B **78**, 155111 (2008).
- ⁴¹ T. Nomura, J. Phys. Soc. Jpn. **83**, 064707 (2014).
- ⁴² J.R. Schrieffer, X.G. Wen and S.C. Zhang, Phys. Rev. B **39**, 11663 (1989).
- ⁴³ N.M.R. Peres and M. A. N. Araújo, Phys. Rev. B, **65**, 132404 (2002).
- ⁴⁴ D. Vaknin, S.K. Sinha, D.E. Moncton, D.C. Johnston, J.M. Newsam, C.R. Safinya, and H.E. King, Jr., Phys. Rev. Lett. **58**, 2802 (1987).
- ⁴⁵ R. Coldea, S.M. Hayden, G. Aeppli, T.G. Perring, C.D. Frost, T.E. Mason, S.-W. Cheong, and Z. Fisk, Phys. Rev. Lett. **86**, 5377 (2001).
- ⁴⁶ P. Blaha, K. Schwarz, G. Madsen, D. Kvasnicka, and J. Luitz, WIEN2k, An Augmented Plane Wave Plus Local Orbitals Program for Calculating Crystal Properties (ISBN 3-9501031-1-2).
- ⁴⁷ A. Shukla, M. Calandra, M. Taguchi, A. Kotani, G. Vankó, and S.-W. Cheong, Phys. Rev. Lett. **96**, 077006 (2006).